Bioactive Materials 12 (2022) 153–168

Contents lists available at ScienceDirect

Bioactive Materials

journal homepage: www.keaipublishing.com/en/journals/bioactive-materials

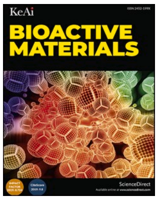

Exhausted local lactate accumulation via injectable nanozyme-functionalized hydrogel microsphere for inflammation relief and tissue regeneration

Jieliang Shen [a], Ao Chen [b], Zhengwei Cai [c], Zhijie Chen [c], Ruichao Cao [a], Zongchao Liu [e,***], Yuling Li [d,**], Jie Hao [a,*]

[a] *Department of Orthopedics, Orthopedic Laboratory of Chongqing Medical University, The First Affiliated Hospital of Chongqing Medical University, No.1 Youyi Road, Chongqing, 40042, PR China*
[b] *School of Biomedical Engineering, Shanghai Jiao Tong University, 1954 Huashan Road, Shanghai, 200030, PR China*
[c] *Department of Orthopaedics, Shanghai Key Laboratory for Prevention and Treatment of Bone and Joint Diseases, Shanghai Institute of Traumatology and Orthopaedics, Ruijin Hospital, Shanghai Jiao Tong University School of Medicine, 197 Ruijin 2nd Road, Shanghai, 200025, PR China*
[d] *Department of Orthopaedics, Affiliated Hospital of North Sichuan Medical College, No.63 Wenhua Road, Nanchong, Sichuan, 637000, PR China*
[e] *Department of Orthopaedics, Affiliated Hospital of Traditional Chinese Medicine, Southwest Medical University, No.182 Chunhui Road, Sichuan, 646699, PR China*

ARTICLE INFO

Keywords:
Hydrogel microsphere
Microfluidic
Lactate
Tissue regeneration
Injection

ABSTRACT

Local lactate accumulation greatly hinders tissue repair and regeneration under ischemic condition. Herein, an injectable microsphere (MS@MCL) for local lactate exhaustion was constructed by grafting manganese dioxide (MnO_2) -lactate oxidase (LOX) composite nanozyme on microfluidic hyaluronic acid methacrylate (HAMA) microspheres via chemical bonds, achieving a long-term oxygen-promoted lactate exhaustion effect and a long half-life *in vivo*. The uniform and porous microspheres synthesized by microfluidic technology is beneficial to *in situ* injection therapy and improving encapsulation efficiency. Furthermore, chemical grafting into HAMA microspheres through amide reactions promoted local enzymatic concentration and activity enhancement. It was showed that the MS@MCL eliminated oxidative and inflammatory stress and promoted extracellular matrix metabolism and cell survival when co-cultured with nucleus pulposus cells (NPCs) *in vitro*. In the rat degenerative intervertebral disc model caused by lactate injection, MS@MCL showed a long-term therapeutic effect in reducing intervertebral height narrowing and preventing extracellular matrix (ECM) degradation as well as inflammatory damage *in vivo*. Altogether, this study confirms that this nanozyme-functionalized injectable MS@MCL effectively improves the regenerative and reparative effect in ischemic tissues by disposing of enriched lactate in local microenvironment.

1. Introduction

Lactate, a double-edged sword for tissue repair and regeneration [1], is crucial to the cellular basis of wound healing, such as cell signaling, angiogenesis and fibroplasia when at a physiological level [2,3]; however, excessive lactate accumulation will recruit inflammatory cells, impair mitochondrial function and promote intracellular reactive oxygen species (ROS) generation, resulting in the death of resident cells which is detrimental to tissue regeneration [4,5], and is particularly critical in the pathogenesis of ischemic diseases. Lactate is continuously produced through anaerobic glycolysis and its local level continues to rise due to the lack of adequate transit route [6]. As the largest avascular tissue *in vivo*, the nucleus pulposus (NP) located in the center of intervertebral disc (IVD) has a hypoxic environment [7] where anaerobic glycolysis is the main energy metabolism for NP cells (NPCs) [8]. In the progress of IVD degeneration (IDD), especially due to the decreased diffusibility of metabolites and nutrients through nearby capillaries [9], the lactate gradually accumulates in the local NP with a concentration

---

Peer review under responsibility of KeAi Communications Co., Ltd.
* Corresponding author.
** Corresponding author.
*** Corresponding author.
E-mail addresses: 565409672@qq.com (Z. Liu), lyl1987@nsmc.edu.cn (Y. Li), hjie2005@aliyun.com (J. Hao).

https://doi.org/10.1016/j.bioactmat.2021.10.013
Received 22 June 2021; Received in revised form 11 September 2021; Accepted 10 October 2021
Available online 21 October 2021

8–10 times as high as that of the surrounding plasma [10]. The lactate accumulation within IVD down-regulates matrix synthesis and promotes NPCs apoptosis [11], causing tissue structural destruction and discogenic pain [12,13]. Therefore, suitable biomaterials are required to efficiently remove local lactate for improving the acidic microenvironment and inhibiting excessive inflammation.

Lactate oxidase enzyme (LOX), a member of the α-hydroxyacid-oxidase flavoenzyme family, enzymatically catalyzes lactate oxidation to generate pyruvate and hydrogen peroxide (H_2O_2) [14]. However, H_2O_2-induced oxidative stress has been confirmed to induce IDD pathogenesis [15], which greatly limits the simple application of LOX for IDD treatment. In addition, the hypoxic condition within NP tissue also impedes the catalytic efficiency of LOX. Therefore, it is a promising strategy to produce oxygen *in situ* by catalyzing the decomposition of endogenous H_2O_2 into oxygen. In recent years, manganese dioxide (MnO_2)-based nanoplatforms have attracted a growing attention to their catalase-like activity to catalyze H^+/H_2O_2 into oxygen (O_2) and Mn^{2+} [16], providing large amounts of enriched oxygen in local areas to facilitate the oxidation catalysis of LOX and alleviate oxidative stress damage from H_2O_2. Herein, a LOX-MnO_2 composite nanozyme is produced via electrostatic adsorption and can achieve O_2-promoted lactate exhaustion through the cyclic reaction to alleviate the lactate-accumulative microenvironment and promote the regeneration of degenerative NPCs. However, the clinical application of this nanozyme has been hindered due to some nonnegligible drawbacks [17]. For instance, exogenous nanozymes can be easily cleared by the intrinsic immune system and are prone to aggregate and precipitate, leading to the fast clearance, structural instability and rapid drug leakage. Due to

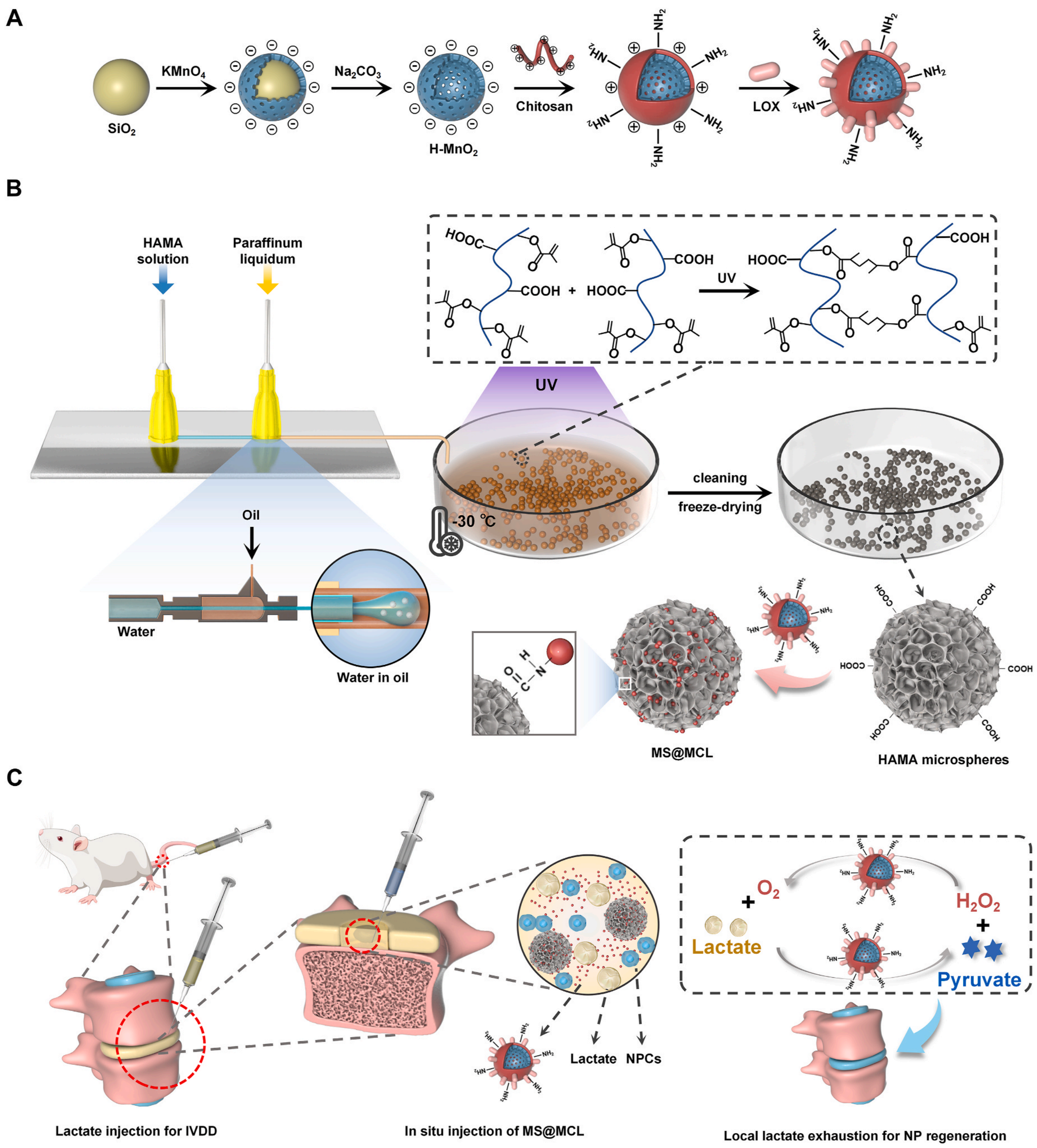

Scheme 1. Schematic illustrations of nanozyme-functionalized hydrogel microsphere and degenerative NP tissue regenerative process. A) Preparation steps of MCL nanozyme. B) Microfluidic fabrication of injectable HAMA microsphere and grafting nanozyme onto microsphere via covalent bond (MS@MCL). C) In situ injection of MS@MCL into rat caudal IDD model for local lactate exhaustion and NP regeneration.

the avascular feature of IVD, injection therapy is the main modality for IDD therapy. Nevertheless, nanoparticles incline to leak and diffuse in the deep tissue *in vivo* due to their small sizes, reducing the efficiency of the targeted therapy. Given this situation, it is imperative to develop ideal matrices supporting the bioactive nanozymes to improve the efficacy of injection therapy for IDD.

Natural and synthetic polymers were applied as insoluble materials for the immobilization of the enzymes [18]. Hyaluronic acid (HA), the main constituent of the extracellular matrix (ECM) in NP tissue [19], has various functional groups that enable the strong enzyme-matrix interactions. Enzyme immobilization can be achieved by binding the enzyme to the activated matrix via chemical cross-linking, with advantages of enhanced enzyme stability, lower production cost, reusability, easy operation and separation [20]. Hydrogel microsphere prepared through microfluidic technology is an appropriate biomaterial for nanoparticle carriers due to its properties of the controllable spatio-temporal release of drugs, efficient encapsulation of nanoparticles and injectability in the deep tissue [21].

In terms of enzyme immobilization strategy, herein, we creatively utilized the uniform-sized porous HAMA microspheres prepared by microfluidic technology to immobilize LOX-MnO_2 nanozymes via covalent binding to synthesize a novel nanozyme-functionalized injectable HAMA microsphere, which ultimately contributes to a suitable microenvironment for IVDs through local lactate exhaustion. As showed in Scheme 1, the MnO_2 nanoparticles were first synthesized with “shell-core” method, and were then coated by chitosan via electrostatic self-assembly to be functionalized with amino groups on the surface. LOX with negative charges was further bonded to the chitosan-coated MnO_2 nanoshells through electrostatic interactions, constructing the MnO_2-Chitosan-LOX (MCL) nanozyme. Meanwhile, photo-crosslinked HAMA microspheres with suitable size and porous structure were prepared by microfluidic technology. Finally, the composite MCL nanozyme was abundantly coupled to the porous microspheres via condensation reaction (denoted as MS@MCL). This innovative nanozyme-functionalized microsphere has advantages of easy production and storage, good injectability and long-term enzyme activity, and has a potential application value in the regenerative treatment for ischemic tissues.

2. Materials and methods

2.1. Preparation of the nanozyme-functionalized hydrogel microsphere

The MnO_2 nanoparticles were first synthesized with modified “shell-core” method [22]. Solid silica nanoparticles ($sSiO_2$) were synthesized through inverse microemulsion method, and then reacted with $KMnO_4$ solution (10 mg/mL) under ultrasonication for 6 h to obtain the mesoporous MnO_2-coated $sSiO_2$. The as-prepared nanoparticles were etched by Na_2CO_3 solution (2 M) at 60 °C for 12 h to obtain the hollow MnO_2 ($HMnO_2$) nanoparticles. Then, Chitosan solution (1 mg/mL dissolved in 1% acetic acid) was pumped to the MnO_2 solution at 0.5 mL/min, meanwhile stirred for 30 min to obtain the positively charged nanoparticles (MC). Next, a certain amount of LOX (20 U) was mixed with the chitosan-coated nanoparticles (2 mg/mL) and shaken for 15 min at 4 °C. The MnO_2-Chitosan-LOX (MCL) nanozyme was obtained by centrifugation and was washed three times with ultrapure water.

Next, the HAMA microsphere scaffolds were prepared using microfluidic technology. HAMA was synthesized according to the method previously reported [23]. Then, 4 wt% HAMA and 0.5 wt% photoinitiator in phosphate buffered saline (PBS) solution as the aqueous phase and 5 wt% Span 80 in paraffin oil as the oil phase are injected into inlets of the microfluidic device through syringes. The flow rate of oil and aqueous phase was adjusted as 10 by a syringe pump. Microspheres were collected in a dish placed in a refrigerating circulator (−30 °C).

Under UV irradiation for 5 min, the generated emulsion droplets were photo-crosslinked, followed by washing with isopropanol and 75% ethanol to remove surfactants and mineral oil. To obtain porous microspheres, the purified microspheres were frozen at −20 °C for overnight and then freeze-dried for 48 h.

Finally, the nanozyme was grafted to the porous microspheres by condensation reaction. Briefly, 100 mg HAMA microspheres were dispersed in 1 mL 2-(N-morpholino)ethanesulfonic acid (MES) buffer (pH = 6) containing 8 mg 1-ethyl-3-(3-dimethylaminopropyl)carbodiimide (EDC) and 12 mg N-hydroxysuccinimide (NHS), and activated at 37 °C for 15 min. The microspheres were added into the as-made nanozymes solution after centrifugation. The condensation reaction was conducted at 37 °C overnight to synthesize nanozyme-functionalized hydrogel microspheres, which were rinsed three times and freeze-dried for further use.

2.2. Nano- and microparticles characterization

The morphology structures of MnO2 and MCL nanoparticles were observed by scanning electron microscope (SEM) (FEI, Sirion 200, USA) and transmission electron microscope (TEM) (FEI, Tecnai G2 spirit Biotwin, USA). The major elements distribution of MnO_2 nanoparticles was exhibited by aberration-corrected scanning transmission electron microscopy in high-angle annular dark field (HAADF-STEM) mode (FEI, Talos F200X, USA) and X-ray Photoelectron Spectrometer (XPS, Kratos, AXIS Ultra DLD, Japan). The particle size and zeta potential of nanoparticles were measured by dynamic light scattering (DLS) (Malvern, Zetasizer Advance Range, UK). UV–vis spectra of different samples were recorded by UV–vis spectrophotometry (ThermoFisher, AquaMate 8100, USA). The expression of LOX on the MCL nanozyme was verified by sodium dodecyl sulfate-polyacrylamide gel electrophoresis assay (SDS-PAGE) (Beyotime, China). In brief, 10 mg MCL Nanoparticles (NPs) solution was mixed with SDS-PAGE loading buffer and heated for 15 min in boiling water. Subsequently, the precipitation and the supernatant were subjected to electrophoresis in 12% SDS-PAGE gel, followed by staining with Coomassie brilliant blue R250. Moreover, the LOX content in MCL was determined by the bicinchoninic acid (BCA) assay. Briefly, 20 μl MCL NPs were incubated directly in the working regent for 1 h at 37 °C. The samples were centrifuged for 5 min at 12000g, and the absorbance of the supernatants was measured at 570 nm. Finally, the content of LOX was quantified according to the standard curve.

The morphology of microsphere samples was measured by phase contrast optical microscope (Nikon, ECLIPSE TS2, Japan), and their diameter was analyzed by Image J software. The microstructure of freeze-dried microspheres was observed using an SEM and a laser scanning confocal microscope (ZSISS, LSM800, Germany). The surface composition detection of MS@MCL was carried out using energy dispersive spectrometer (EDS) (JEOL, JSM-7800F, USA). The degradation of HAMA microspheres was conducted in PBS-containing hyaluronidase that mimics the *in vivo* physiological environment. Briefly, 10 mg MS@MCL microgels were dispersed in 1 mL PBS (pH ~ 7.4, 37 °C), with 0.1 U/mL hyaluronidase replenished every day to maintain hyaluronidase activity. At the predetermined time points, the degradation of MS@MCL was observed according to morphological changes and analysis of remaining weight. The residual weight (RW) was calculated by the following formula:

$$\mathrm{RW}\ (\%) = \mathrm{RW\ at\ T_x / \ original\ weight}$$

Where T_x refers to predetermined time point X.

Fourier transform infrared spectroscopy (FTIR) was performed to characterize the chemical bonds present in the samples. A total of 128 scans were accumulated for each spectrum at a 4 cm^{-1} resolution with the wave number range of 4000–1000 cm^{-1} by KBr pellet technique.

Meanwhile, the MnO_2 and LOX loading capacity of MS@MCL were quantitatively evaluated by inductively coupled plasma mass spectrometry (ICP-MS) and BCA protein assay, respectively. The loading efficiency (LE%) can be calculated as follows:

$$\mathrm{LE\%} = (\mathrm{M1\text{-}M2})/\mathrm{M1} \times 100\%$$

Where M1 is the original cargos content and M2 is the remaining cargos content. Then, the enzyme activity of free MCL and immobilized MS@MCL were obtained by high performance liquid chromatography (HPLC). Briefly, a proper amount of MCL or MS@MCL was added into 40 mL 5% lactate solution prepared by Tris (hydroxymethyl) aminomethane hydrochloride (Tris-HCl) (0.1 mol/L, pH 7.4 or 5.5) containing 0.5 mL catalase at 37 °C, and the catalytic reaction lasted 10 min with the oxygen flow (0.7 L/min). Then, 1 mL reaction solution was collected for the quantification of pyruvate by HPLC. The relative activity was calculated and compared by using the standard activity assay procedure mentioned following:

$$\text{Relative activity (\%)} = A_i/A_{standard}$$

where A_i is the activity of every sample at preset time intervals or pH value and $A_{standard}$ is the activity of the sample at above-mentioned condition.

The lactate consumption effect was assessed by Lactic Acid assay Kit (DOJINDO, Japan). All dissolved oxygen detection experiments were conducted in the environment sealed with liquid paraffin by dissolved oxygen meter (REX, JPSJ-605F, China). To detect the Mn^{2+} release in simulated IDD microenvironment, MS@MCL were dispersed into the PBS solution (10 mM, pH 7.4) and lactate buffer solution (10 mM, pH 5.5) with or without the presence of H_2O_2 (1 mM), respectively. The dialysate samples were collected at different time points and detected by ICP-MS or magnetic resonance imaging (MRI) (Bruker, Avance III HD 400, Germany) with T1-weighed signal.

NPCs isolation and culture: The NPCs used in this study were extracted from the caudal vertebrae in Sprague-Dawley rats. The NP tissues were extracted and sequentially digested by 0.25% trypsin solution and 0.2% type II collagenase (sigma, USA) at 37 °C for 3–5 h. Then, the tissue debris was removed by a 200-μm filter and the NPCs were resuspended in Dulbecco's Modified Eagle Medium/Nutrient Mixture F-12 (DMEM/F12) medium with 10% fetal bovine serum (Gibco, USA). The cells were cultured in an incubator containing 5% CO_2 at 37 °C, and the third passage of NPCs was used in *in vitro* studies.

2.3. *Co-culture of microspheres and NPCs*

The *in vitro* cytotoxicity was first detected by cell counting kit-8 (CCK-8) assay. The third generation of NPCs were seeded in 96-well plate (5×10^3 cells per well) and cultured overnight, then the cells were treated with MS@MCL containing 0–500 μg/mL MnO_2 for 24 h with or without lactate pretreatment. After intervention, 10 μl CCK-8 solution (Beyotime, China) was added and incubated for 3 h. A microplate reader (Molecular Devices, USA) was used to detect the absorbance at 450 nm, with the cell viability as a percentage of the control group.

To mimic the lactate-rich environment, NPCs were incubated with 6 mM lactate solution and co-cultured with MS@MCL, MCL or MS for 72 h in a Transwell-Permeable Support (TPS) with 0.4 μm pore polyester membrane (Corning, USA). Then, a live/dead staining assay (Thermo Fisher, USA) was performed to assess the viability of NPCs according to the manufacturer's protocol. Briefly, NPCs (1.5×10^4/mL) were cultured on the lower chambers of the 24-well plates while the biomaterials were in the upper TPS. On day 3, the cells were incubated with 250 μL Calcein-AM/propidium iodine (PI) detection working solution (Beyotime, China) for 30 min and subsequently observed under a fluorescent microscope, in which intact viable cells appeared green and the dead cells with damaged plasma membranes are stained red. Cell viability was measured in three randomly chosen stacks. Stacks were split into single color channel images, and the number of green and red dots were counted with ImageJ software. The intracellular ROS levels were tested by staining with ROS probe 2,7-Dichlorodi-hydrofluorescein diacetate (DCFH-DA) (5 μM) for 10 min. All samples were captured by fluorescence microscope (ZEISS, Axio Observer A1, Germany).

The expressions of aggrecan and collagen type II, the major components within the discs, were detected by immunofluorescence staining. Briefly, cell slides were fixed in 4% paraformaldehyde, permeabilized with Triton X-100, and blocked with 5% bovine serum albumin (BSA). Then, they were incubated with the aggrecan and collagen type II primary antibodies at 4 °C overnight. On the second day, the cells were incubated with a fluorescent secondary antibody and DAPI after washing, and were observed by fluorescence microscope. The expression of inflammation and ECM-related genes were analyzed by quantitative real-time PCR. Relative expression levels of the indicated genes were calculated using the $2^{-\Delta\Delta}$Ct method. Primers for the amplification of genes were synthesized by Takara (Japan) and are listed in Table S1.

2.4. *Transcriptomic analysis*

3 days after the co-culture with MS@MCL under lactate stimulation, the RNA of NPCs was extracted by serial TRIzol-chloroform extractions. The high-throughput sequencing was conducted in Matware BioTech Co., Ltd. Feature Counts v1.6.2 was used to calculate the gene alignment, and the fragments per kilobase per million (FPKM) of each gene was then calculated based on the gene length. DESeq2 v1.22.1 was used to analyze the differential expression between the two groups, and the P value was corrected using the Benjamini & Hochberg method. The enrichment analysis is performed based on the hypergeometric test. For the Kyoto encyclopedia of genes and genomes (KEGG), the hypergeometric distribution test was performed in the unit of pathway. Additionally, Cytoscape software (Version 3.4.0, http://www.cytoscape.org/) was utilized for constructing the protein-protein interaction (PPI) network. Degree $\geq$20 was set as the cutoff criterion. The Molecular Complex Detection (MCODE) app was used to analyze PPI network modules.

2.5. *Establishment of rat caudal IDD models*

Eight-week-old SD rats obtained from the Shanghai JieSiJie Laboratory Animals Co., LTD were used to establish the caudal IDD models. Animal experimental protocols were approved by the Ethics Committee for Animal Experimentation of the Ruijin Hospital of Shanghai Jiao Tong University. Rat tails were sterilized after complete anesthesia by 10% chloral hydrate, then Co5~10 IVDs were punctured sequentially with 26G needles and microsyringes to inject 1 μL lactate solution (6 mM) for each IVD, except for the Co5/6 disc as sham-operated group. Each disc was then injected with 20 μL microsphere or nanozyme solution 3 days after lactate injection, except for the Co9/10 level as the control group which was injected with PBS. A supplementary injection of lactate with the same dose was added 4 weeks after the first injection. According to this strategy, each tail received 5 different processings as following: 20 μL of PBS, MS@MCL (0.4 mg/kg MnO_2), MCL (0.4 mg/kg MnO_2), MS (100 mg/mL) and sham opearation, respectively. At set time point, 3 rats were euthanized to get intervertebral disc samples for each analysis.

2.6. *Radiological evaluation*

X-ray and MRI examination were performed 4 and 8 weeks after the first injection. For X-ray evaluation, changes in the disc-height index (DHI) of treated discs were calculated as DHI% and were compared with the values of normal discs; For MRI evaluation, Pfirrmann grades according to T2-weighted section images were used to assess the degree of IVD.

2.7. *Histological evaluation*

Samples were collected 4 and 8 weeks after first injection and were conventionally decalcified for paraffin embedding. Then, the samples were cut into 5 μM slices, which were used to compare the changes in intervertebral disc structure by hematoxylin-eosin staining (HE) staining, observe collagen remodeling and composition by Saffron O staining and quantify the expression of Collagen type II and IL-1β by immunohistochemistry.

2.8. *Statistical analysis*

The results of quantitative data were shown as mean ± standard deviation (SD) values.

The results were analyzed statistically by one-way ANOVA followed by Tukey's post hoc test by Statistical analysis (SPSS Software, USA). When the p value of the *t*-test is less than 0.05, it is defined as a significant difference.

3. Results

3.1. *Characterization of the MnO2-LOX nanozyme*

The topographical features of $HMnO_2$ nanoparticles were first characterized by SEM and TEM. It was shown that $HMnO_2$ had a uniform spherical and hollow structure with the diameters of about 100 nm (Fig. 1A and B), and the thickness of such MnO_2 shell was measured to be ~10 nm (Fig. 1C). Besides, the chitosan coating and LOX loading hardly affected the morphological structure and average diameter of $HMnO_2$ nanoparticles (Fig. 1D and G). To further verify the validity of $HMnO_2$

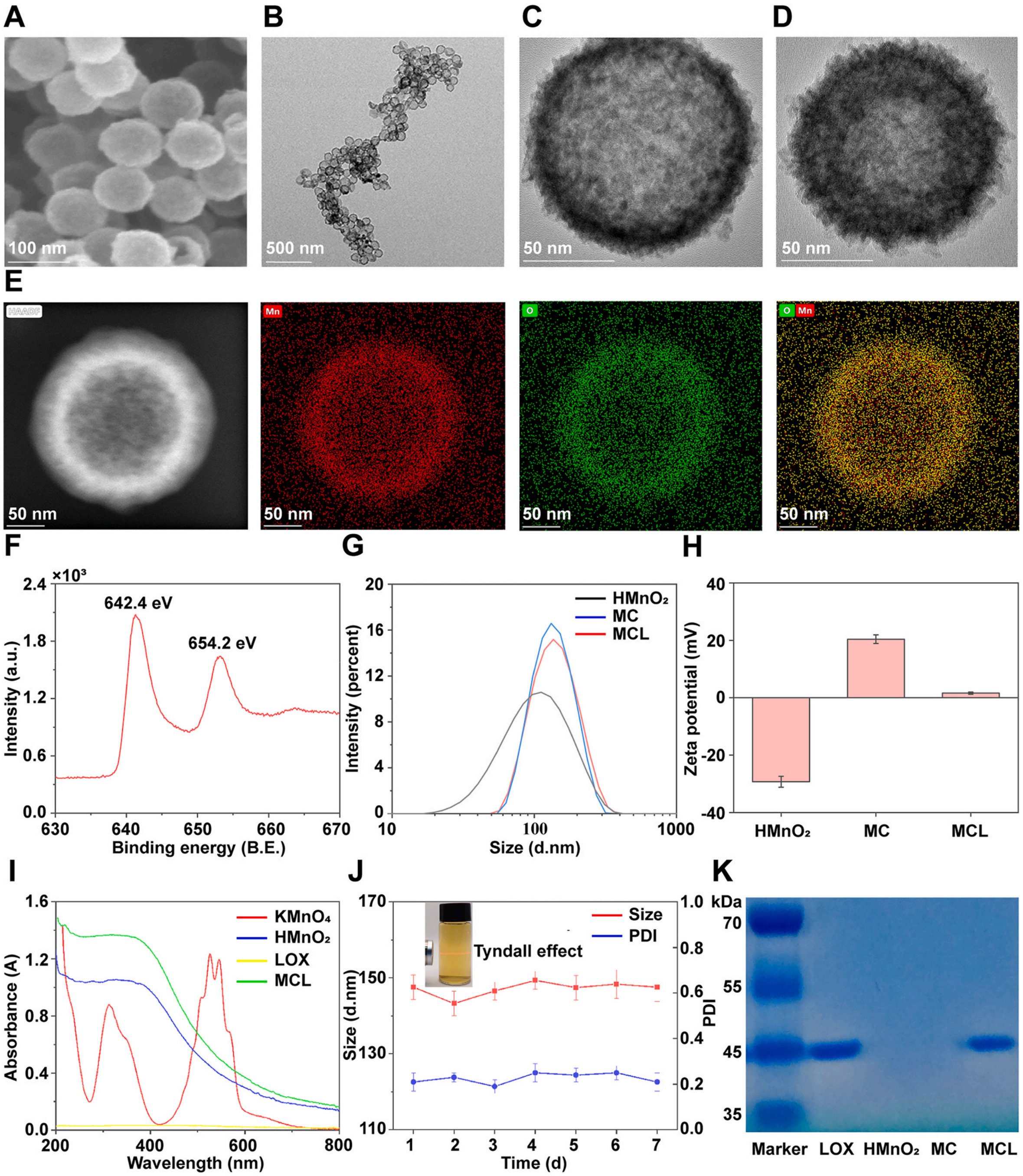

Fig. 1. Characterization of MCL nanozyme. A) SEM image of $HMnO_2$ nanoparticle. B, C) TEM images of $HMnO_2$ nanoparticles, D) and MCL nanoparticles. E) HAADF-STEM images of $HMnO_2$ nanoparticles. F) XPS analysis of $HMnO_2$ nanoparticle. G, H) Size distribution and Zeta potentials of different samples detected by DLS. I) UV–vis absorption spectra of the intermediate products during the preparation process of MCL nanozyme. J) Size and PDI data of MCL nanozyme in saline solution for one week. K) SDS-PAGE protein analysis of LOX, $HMnO_2$ nanoparticles, chitosan-coated $HMnO_2$ nanoparticles (MC) and MCL nanozyme.

nanoparticles, HAADF-STEM was used to display the distribution of the major elements. As expected, Manganese (Mn) and Oxygen (O) were found to be distributed peripherally in the sample (Fig. 1E). The XPS spectrum showed the spin-orbit peaks at 654.2 and 642.4 eV which corresponded to Mn (IV) $2p_{2/3}$ and Mn (IV) $2p_{1/2}$, conforming the formation of +4 valence state of manganese in the nanoparticles (Fig. 1F). The zeta potentials of intermediate products changed obviously (Fig. 1H) and the UV–vis spectra were recorded (Fig. 1I), of which the peaks at 525–545 nm for the characteristic spectrum of $KMnO_4$ disappeared in $HMnO_2$ samples instead of showing a broad-spectrum absorption; while the spectrum between $HMnO_2$ and MCL was similar, indicating that the introduction of chitosan and LOX had no effect on the property of MnO_2. Specifically, during the preparation process, the different intermediate products were identified by zeta potentials and UV–vis spectra, indicating the successful modification of MCL at each step. The synthesized MCL nanoparticles are colloidal in the aqueous solution, and the solution exhibits an obvious "Tyndale" effect. As shown in Fig. 1J, MCL demonstrated good stability in saline solution

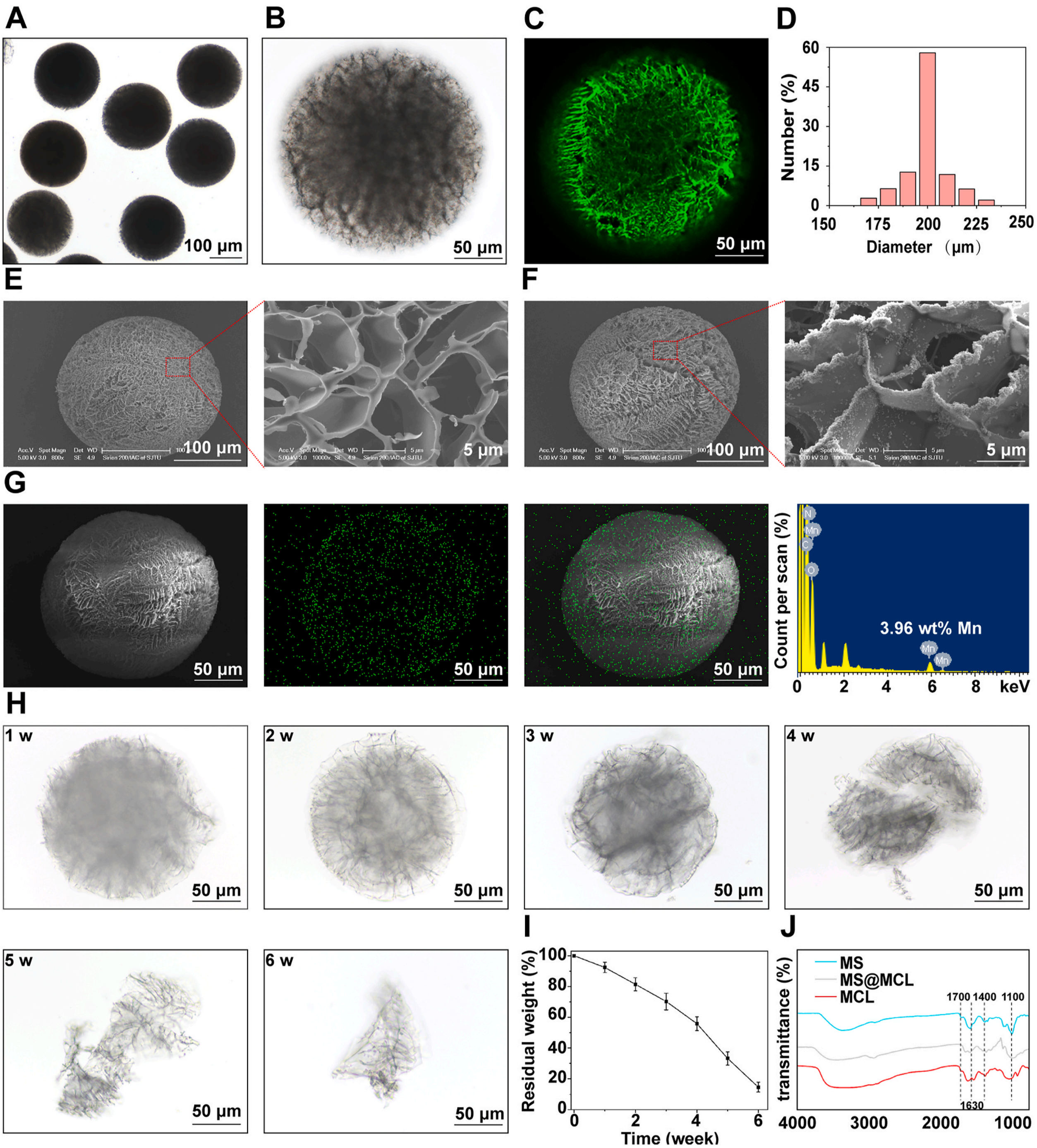

Fig. 2. Physical characterization of MCL nanozyme-grafted microsphere. A, B) Microscopy images of MS@MCL. C) Laser confocal microscopy images of MS@MCL. FITC-labeled MCL exposed on the surface of microspheres were displayed with strong green fluorescence. D) Particle size of MS@MCL microsphere. E) SEM image of HAMA microsphere before grafting MCL nanozyme. F) SEM image of HAMA microsphere after grafting MCL nanozyme. G) EDS mapping image of Mn elements of MS@MCL. H) The microscopy images of the morphological change of MS@MCL over 6 weeks. I) The degradation curve of MS@MCL. J) FTIR analysis of different samples. (For interpretation of the references to color in this figure legend, the reader is referred to the Web version of this article.)

with negligible changes in the hydrodynamic diameter (Dh [Particle size]) and polydispersity index (PDI) for a week. However, MCL exhibited time-dependent degradation behavior in lactate solution (pH 5.5) due to the decomposition of MnO_2 into Mn^{2+} ions (Fig. S1). Finally, the protein of LOX retained on the MCL nanopariticles was verified by SDS-PAGE assay, with the loading capacity of LOX as 22.94 μg/mg (Fig. 1K).

3.2. *Characterization of nanozyme-functionalized microspheres*

The HAMA microspheres were formed through a water-in-oil method using a microfluidic device, whose size could be adjusted by the flow rate of oil/water phase. Previous literature indicated 26-gauge (26 G) needle puncture would not lead to IDD model [24], so we adjusted the oil/water phase flow rate as 10 to obtain uniform microspheres with a diameter of approximate 200 μm to pass through the microsyringe needle smoothly without damage (Video.S1 and Fig. S2). Furthermore, the original HAMA microspheres were photo-crosslinked at −30 °C and then freeze-dried to sublime the internal ice crystal to obtain porous structure. These as-made microspheres showed good dispersibility and uniform size under the light microscope at low magnification (Fig. 2A), and the internal porous structure was observed at high magnification (Fig. 2B). Then, the carboxyl groups of HAMA microspheres were activated by EDC/NHS reaction, followed by being covalently linked to the amino residue on the MCL nanozyme to form MS@MCL microsphere. FITC-labeled MCL nanoparticles exposed on the surface of microspheres displayed strong green fluorescence under laser confocal microscopy (Fig. 2C), which clearly outlined the internal porous structure (Fig. S3), indicating the effective immobilization of nanozymes onto the microsphere network. The average particle size was approximately 198.64 ± 15.21 μm, ranging from 170 μm to 230 μm (Fig. 2D). As shown by SEM, the HAMA microspheres exhibited a porous structure, which would increase the loading of MCL nanozyme (Fig. 2E and F). The Mn element of MS@MCL was illustrated in the EDS mapping images, which accounted for about 3.96% of the total mass (Fig. 2G). To mimic the gradual degradation process *in vivo*, MS@MCL microgels were incubated with 0.1 U/mL of hyaluronidase in PBS solution at 37 °C for six weeks. In the first three weeks, the general shape of microspheres remained intact, with the volume gradually shrinking; in the fourth week, the morphology started to collapse with irregular margins and cracks; in the

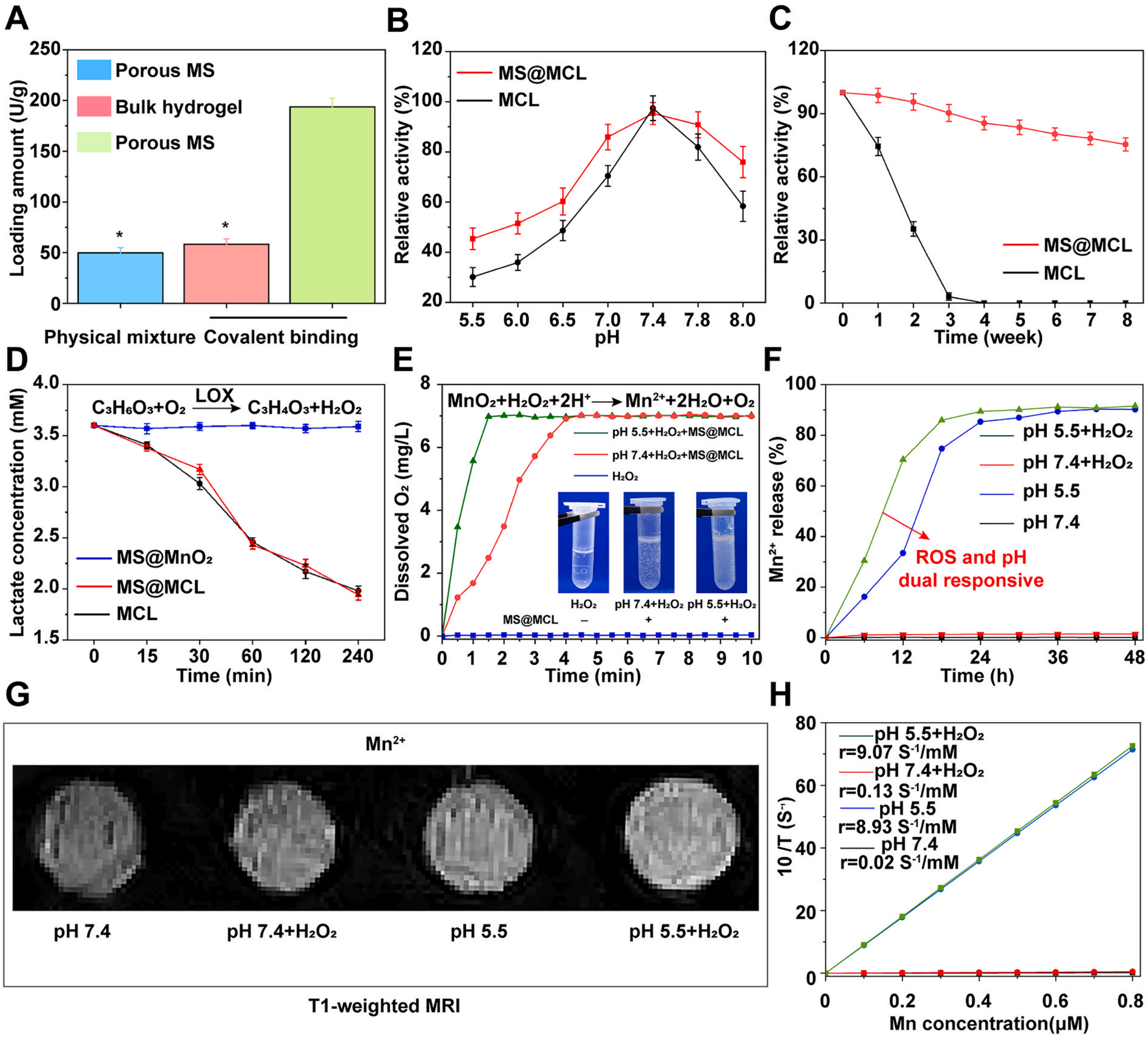

Fig. 3. Functions verification of MS@MCL *in vitro*. A) Comparison of the loading amount of LOX among different bonding forms. B) Comparison of the enzymatic activity between immobilized and free MCL under different pH conditions. C) Comparison of the heat stability between immobilized and free MCL. D) Comparison of the lactate consumption effect among $MS@MnO_2$, MS@MCL and MCL. E) Dissolved oxygen profiles of the mixed solution of MS@MCL and H_2O_2 at pH 7.4 and 5.5. F) Mn^{2+} release profiles of MS@MCL under different conditions. G) T1-weighted MRI of Mn^{2+} from MS@MCL under different conditions. H) The fitting curve of longitudinal relaxivity and Mn^{2+} concentration.

sixth week, the residual structure persisted, which was favorable for maintaining a long-term local high nanozyme concentration (Fig. 2H). Consistent with the morphology changes, the residual weight of MS@MCL microspheres slightly decreased over time. Moreover, as shown in FTIR analysis, stretching vibrations of C═O at 1700 cm^{-1} and C–O at 1100 cm^{-1} were characteristic of HA; peak at 1630 cm^{-1} in the MCL and MS@MCL groups were characteristic of amino I; a new peak that appeared at 1400 cm^{-1} in MS@MCL was assigned to a C–N stretching vibration, indicating the successful nanozymes grafting (Figure.2J, Fig. S4).

In order to compare the immobilization efficiency of different carriers and grafting approaches, the MCL nanozymes were combined onto porous microspheres and bulky hydrogels through physical mixing or chemical bonding, respectively. The results showed that the amount of LOX loaded on porous microspheres through in-situ condensation reaction was up to 193.67 U/g, which was significantly higher than that in the other two groups (Fig. 3A). Furthermore, the loading capacity of MS@MCL for MnO_2 was 63.48 mg/g, and the loading efficiency of MnO_2 and LOX in MS@MCL microspheres was 91% and 93%, respectively. The HAMA microspheres limited the diffusion of encapsulated MCL via covalent bonding, providing an attractive method for controlled and sustained local nanozymes delivery. However, the effect of this chemical cross-linking approach on the enzyme activity still needs to be tested. The enzyme activity of immobilized MS@MCL and free MCL was first compared in the range of pH 5.5–8.0 (Fig. 3B). Optimal pH of immobilized MS@MCL and free MCL was found as 7.4, but the activity of immobilized enzyme at each pH value was stronger compared to the free enzyme, which indicated that the immobilization method retains enzyme activity over a wider pH range. Meanwhile, the heat stability of the immobilized enzyme significantly improved in water bath at 37 °C. As shown in Fig. 3C, enzyme in the free MCL almost lost its activity within 4 weeks. In contrast, the immobilized MS@MCL maintained 75.36% of enzyme activity after 8 weeks. Nanozyme immobilized to microspheres was more resistant to pH and heat inactivation mainly due to covalent bonding via amido linkage [25]. These results indicated that the nanozyme inside the microsphere could remain stable for a long time.

To further evaluate the lactate consumption activity, the dialysis bag containing the same amount of free MCL or immobilized MS@MCL was soaked into lactate solution and shaken at 37 °C, and the dialysate samples were taken at the set intervals for lactate detection. The lactate concentrations in the dialysate gradually decreased synchronously in both groups, implying that the immobilized MS@MCL maintained the catalytic activity of LOX (Fig. 3D). However, with lactate consumption, H_2O_2 produced by oxidative catalysis of lactate would lead to severe oxidative stress on NPCs. The catalase-like ability of MnO_2 for removing H_2O_2 could be verified by detecting the production of O_2 and Mn^{2+} [26]. After mixing exogenous H_2O_2 with MS@MCL, dissolved oxygen evaluated at both pH 7.4 and 5.5 demonstrated that more oxygen was generated in acidic conditions, effectively alleviating the local hypoxic environment and providing favorable conditions for the oxidation and removal of lactate (Fig. 3E). In contrast, lactate oxidation reaction without H_2O_2 addition would accelerate oxygen consumption with the increase of lactate concentration that could aggravate the hypoxic state (Fig. S5). As shown in Fig. 3F, with the presence of both H_2O_2 and H^+, Mn^{2+} decomposed from MnO_2 was rapidly released from MS@MCL microsystem. Meanwhile, a mass of Mn^{2+} ions were also generated by the decomposition of MnO_2 in lactate solution (pH 5.5) without exogenous H_2O_2 because continuous H_2O_2 was generated since LOX could catalyze lactate into H_2O_2 efficiently. In contrast, a small amount of Mn^{2+} was detected in PBS solution at pH 7.4 with H_2O_2 treatment. Moreover, as the release of Mn^{2+} and LOX, the pH of lactate solution increased from 5.5 to 7.5 due to proton consumption when MnO_2 reacted with H_2O_2 (Figs. S6 and S7). All these results demonstrated that MS@MCL might exhibit microenvironment-sensitive effects in IDD, since ischemic tissues are rich in lactate with a reduced pH. Consistent with the release results of Mn^{2+}, a decreased $T1$ signal was detected in the MS@MCL sample without H_2O_2 treatment, and the initial longitudinal relaxivity $r1$ at pH 7.4 and pH 5.5 was only 0.02 and 0.03 mm^{-1} s^{-1}, respectively. While in an acidic environment, the $T1$ signal was enhanced after H_2O_2 treatment, and the initial longitudinal relaxivity $r1$ increased to 9.07 mm^{-1} s^{-1} (Fig. 3G and H). All these results demonstrated that composite MCL nanozyme grafted to HAMA microspheres had good reactivity in acidic and ROS conditions and had potential application prospects in the repair and regeneration of IDD, since NP tissues overexpressed endogenous H_2O_2 and the extracellular microenvironment of NPCs was acidic.

3.3. *In vitro promoting regeneration assessment*

The extracellular lactate accumulation plays an important role for promoting NPCs apoptosis [27], matrix degradation [11], mechanical compression [28], and inflammation [29]. To reduce lactate level, the MS@MCL microspheres were co-cultured with NPCs in a lactate-rich microenvironment. Fig. 4A shows the extracellular lactate exhaustion process of MS@MCL cascade catalytic effect at cellular level. First, the cytotoxicity of MS@MCL against NPCs was analyzed by CCK-8 assay in normal complete medium. As shown in Fig. S8, inappreciable cytotoxicity against NPCs was observed in MCL NPs with different MnO_2 concentrations; in addition, the MS@MCL demonstrated a concentration-dependent cytoprotection against lactate treatment, which at the concentration of 100 μg/mL had a definite cytoprotective effect in the presence of lactate. Thus, the 100 μg/mL concentration was chosen for subsequent experiments.

By further staining with Live/Dead cell dye solution, a significantly smaller proportion of dead cells (red) were observed in MCL and MS@MCL groups, suggesting the presence of MCL nanozyme could prominently protect the NPCs from lactate-accumulative microenvironment *in vitro* (Fig. 4B and D). In addition, the protective function of these nanozyme-functionalized microspheres on NPCs against the noxious ROS was also investigated in the pathological acidic microenvironment. The Bio-TEM observation revealed that the endocytosed MCL nanoparticles were observed in the lysosomes of NPCs (Fig. S9), and the intracellular ROS variations detected through a ROS indicator DCFH-DA showed that NPCs co-incubated with MCL or MS@MCL exhibited obviously lower green fluorescence compared to the other control groups, suggesting that the free or immobilized MCL could effectively attenuate the lactate-induced oxidative stress *in vitro* (Fig. 4C and E).

The degradation of extracellular matrix, loss of bound water molecules, decreased tissue osmotic pressure and resulting mechanical failure of the disc are the major features of IDD [30]. The ECM of NP is mainly constituted by aggrecan and collagen type II, which were further examined by immunofluorescence staining experiments. The aggrecan and collagen type II associated fluorescence intensity was significantly lower in lactate-treated group, demonstrating ECM synthesis ability of NPCs significantly decreased in lactate-rich condition. Conversely, the opposite trend was observed in aggrecan and collagen type II staining in MCL and MS@MCL groups, demonstrating lactate exhaustion was in favor of promoting NPCs viability to maintain ECM synthesis (Fig. 5Ã5D). The findings of RT-PCR showed that lactate treatment induced the overexpression of inflammatory cytokines such as IL-1β and TNF-α at the gene expression level. Inflammatory processes, exacerbated by TNF-α and IL-1β, are believed to be critical events during IDD [31]. More and more evidence has confirmed that lactate is emerging as an important signaling molecule promoting specific immune-inflammatory responses, which is consistent with our results. However, MS@MCL microspheres were able to down-regulate the expression of inflammatory cytokines through the delivery of the LOX-MnO_2 nanozyme. Interestingly, the expressions of IL-1β and TNF-α also slightly decreased in HAMA microsphere group, suggesting the anti-inflammatory effect of hyaluronic acid for IDD treatment (Fig. 5E and F). Furthermore, the

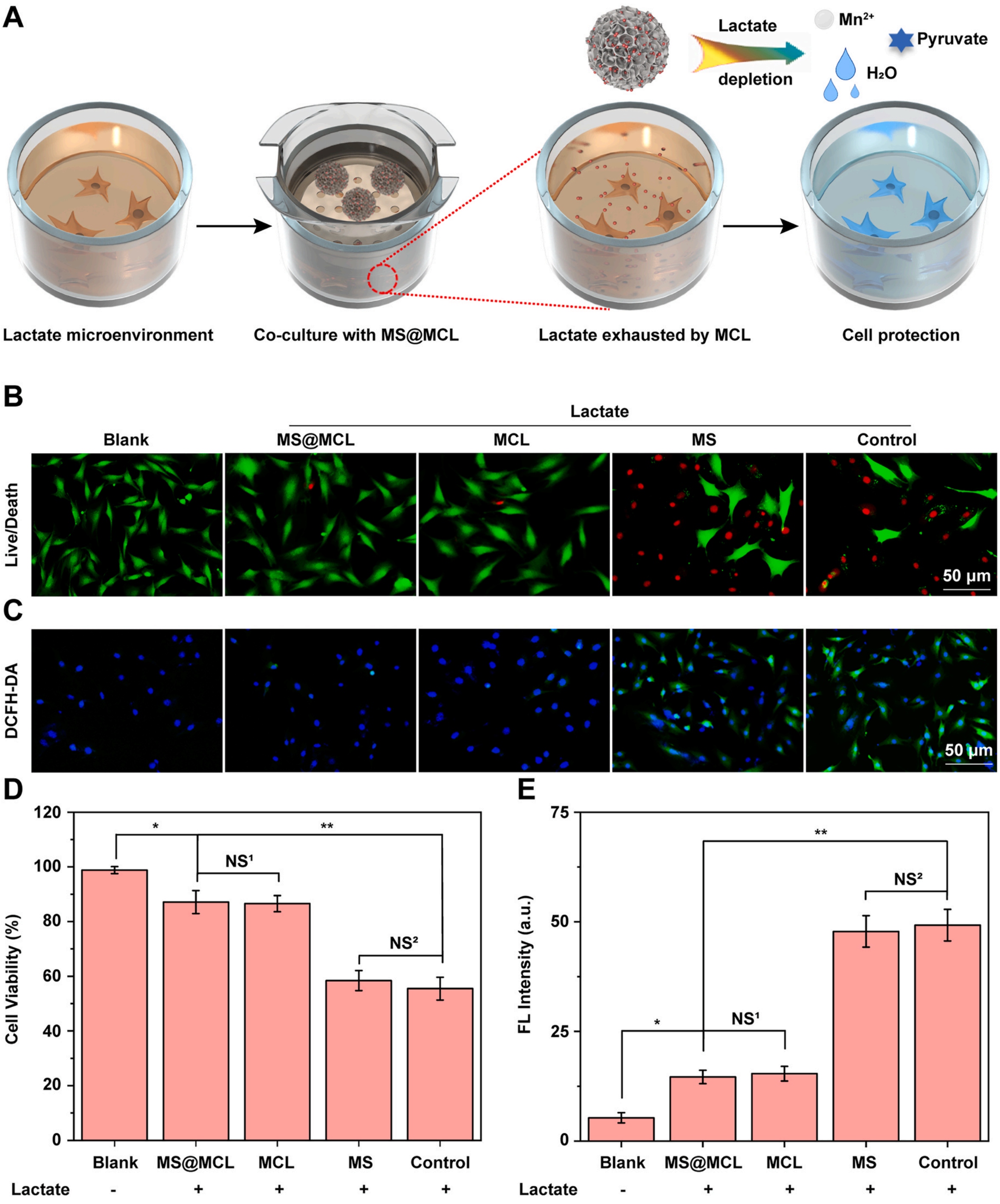

Fig. 4. Enhanced NPCs survival by alleviating oxidative stress under lactate stimulation. A) Schematic diagram of exhauting lactate by MS@MCL co-cultured with NPCs. B) The *in vitro* NPCs survival detected by Live/Dead staining (green fluorescence, Calcein AM indicates live cells; red fluorescence, propidium iodide indicates dead cells). C) The alleviation of oxidative stress in NPCs monitored via a ROS probe (DCFH-DA) after different treatment. D, E) The quantitative studies of cell viability and ROS depletion analyzed by counting the fluorescent intensity of NPCs, respectively. *p Vs. MS@MCL group <0.05, **p Vs. MS@MCL group <0.001, NS^1 Vs. MS@MCL group, not significant, NS^2 Vs. MS group, not significant. (For interpretation of the references to color in this figure legend, the reader is referred to the Web version of this article.)

expressions of catabolism related genes of ECM in NPCs such as the MMP3, MMP13 and ADAMATs-5 were also down-regulated; and the expression of protease inhibitor TIMP-1 was significantly increased because of lactate elimination (Fig. 5G~5J). The above results suggested that MS@MCL microspheres could inhibit lactate-mediated inflammation and ROS, promote the activity of NPCs and up-regulate the expression of extracellular matrix, which was beneficial to the repair and regeneration of IDD, but the underlying molecular mechanism needs to be further studied.

It was reported that lactate could cause inflammatory response via various mechanisms, such as revitalizing T and NK cells, promoting cell pyroptosis, as well as activating NF-κB pathway to increase proinflammatory cytokines [32]. Thus, NPCs cultured in lactate-rich microenvironment with or without MS@MCL were collected for transcriptomics analysis. A total of 16,436 genes of NPCs were analyzed, and the gene expression relationship between two groups was exhibited

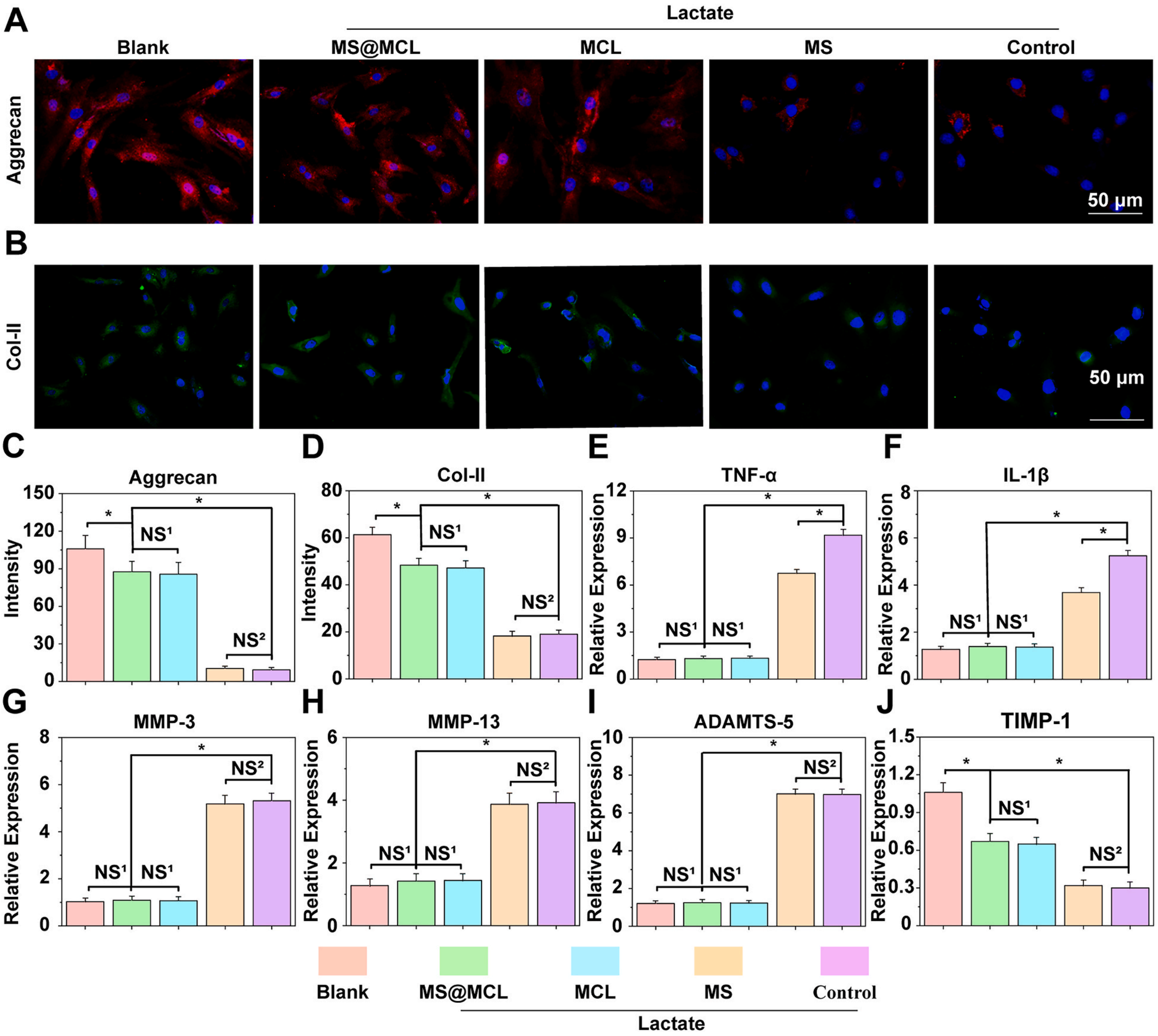

Fig. 5. Enhanced extracellular matrix synthesis and alleviated inflammatory response under lactate stimulation. A, B) Immunofluorescence analysis of aggrecan and COL-II expressions of NPs under different treatments. C, D) The semi-quantitative analysis of aggrecan and COL-II mRNA expressions. E, F) The semi-quantitative analysis of major inflammatory factors, TNF-α and IL-1β mRNA expressions. G, H, I, J) The semi-quantitative analysis of matrix metabolic enzymes, MMP-3, MMP-13, ADAMTS-5 and TIMP-1 mRNA expressions. *p Vs. MS@MCL <0.05, NS^1 Vs. MS@MCL group, not significant, NS^2 Vs. MS group, not significant.

by the volcano plot, of which 1484 up-regulated and 1795 down-regulated genes were screened with the threshold of fold change ≥2 and $p < 0.05$ (Fig. 6A). The genes related to "inflammatory activation" were further screened to evaluate the cellular immunity of NPCs, demonstrating that most of inflammation activation related proteins were significantly down-regulated in the MS@MCL group (Fig. 6B). After that, GO enrichment bubble plots represented all differentially expressed genes. The biological pathway, cellular component and molecular function were represented as red, blue and grey circles, respectively. Top 5 enrichment terms for each category were shown (Fig. 6C). The immune-related genes were analyzed by KEGG enrichment analysis to study the inflammatory pathway induced by lactate accumulation. Furthermore, the enrichment of specific genes in aforementioned pathways were showed in Fig. S10A. As showed in Fig. 6D, inflammatory response activated by lactate stimulation was mainly dependent on the "P53", "MAPK", "cell cycle" and "peroxisome" pathways. Then, crucial genes were identified using molecular complex detection (MCODE) (a plugin in Cytoscape), of which the network cluster included genes in MFKB pathway, including ErbB2, Gsk3b, Ptgs2. As shown in Fig. 6E, most of the genes corresponded to co-expression and were involved in the cellular response to inflammation, and the gene-gene interaction network was shown in Fig. S10B. Together, MS@MCL microspheres exhibited excellent regulation ability for lactate-rich microenvironment, which might contribute to improving the therapeutic effect of IDD through reducing the local inflammatory reaction.

3.4. *In vivo therapeutic effect for a lactate-induced rat IDD model*

Despite the similar cytoprotective effect of free and immobilized MCL on NPCs *in vitro*, they were injected into the rat IDD model to compare the *in vivo* therapeutic effect on promoting IDD regeneration. The rat IDD model was established by injecting lactate solution (6 mM) into the IVDs through 26 G needles and microsyringes. In order to simulate the microenvironment of long-term lactate accumulation *in vivo*, the supplementary lactate was injected 4 weeks after the first injection. The imaging and histological evaluations were used to reflect the degeneration or regeneration of IVD (Fig. 7A). Toxicity study was also performed. The rats were sacrificed 4 weeks after first treatment and major tissues were peeled off for biosafety analysis. HE staining showed the negligible damage area found in the major organs,

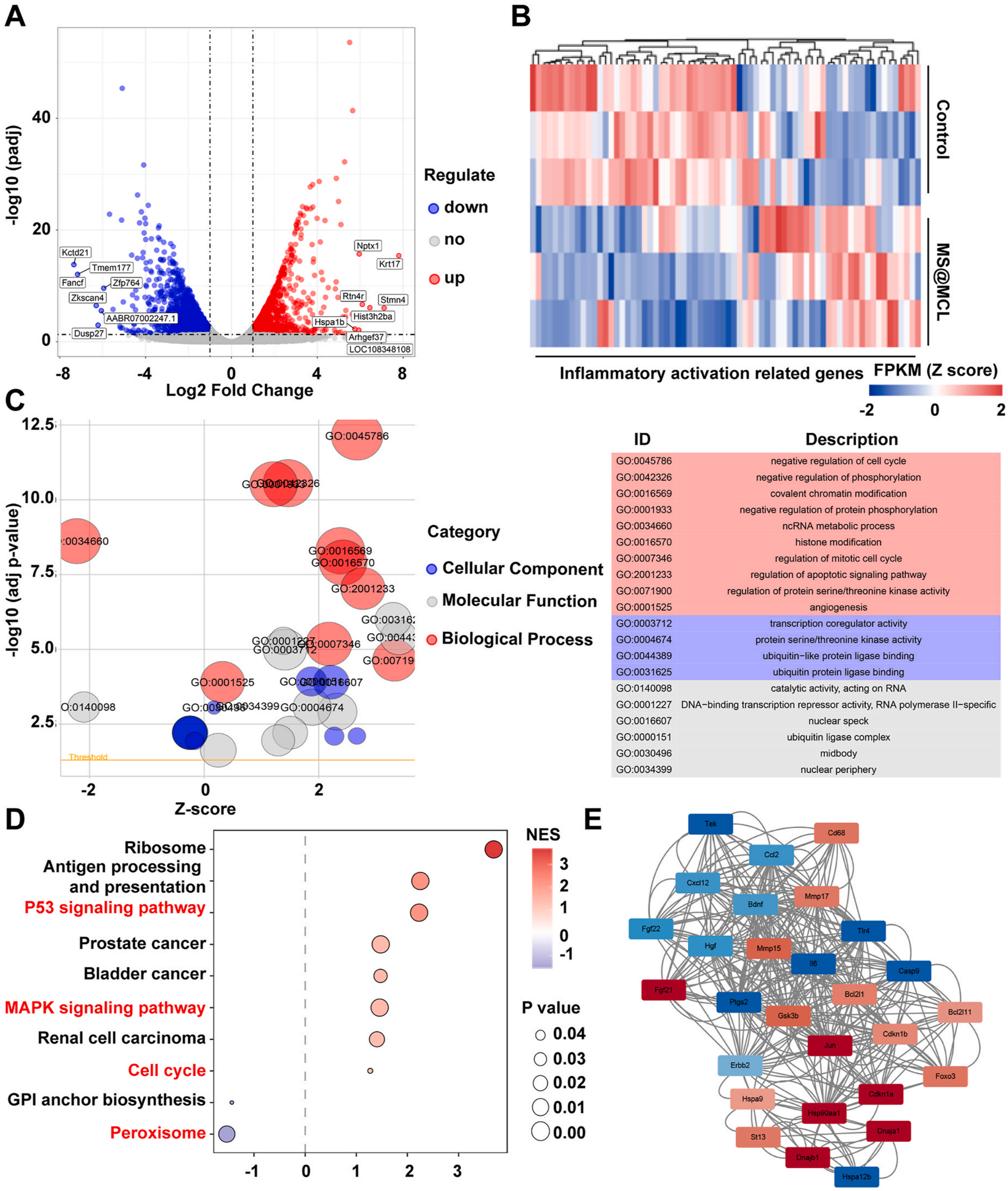

ID	Description
GO:0045786	negative regulation of cell cycle
GO:0042326	negative regulation of phosphorylation
GO:0016569	covalent chromatin modification
GO:0001933	negative regulation of protein phosphorylation
GO:0034660	ncRNA metabolic process
GO:0016570	histone modification
GO:0007346	regulation of mitotic cell cycle
GO:2001233	regulation of apoptotic signaling pathway
GO:0071900	regulation of protein serine/threonine kinase activity
GO:0001525	angiogenesis
GO:0003712	transcription coregulator activity
GO:0004674	protein serine/threonine kinase activity
GO:0044389	ubiquitin−like protein ligase binding
GO:0031625	ubiquitin protein ligase binding
GO:0140098	catalytic activity, acting on RNA
GO:0001227	DNA−binding transcription repressor activity, RNA polymerase II−specific
GO:0016607	nuclear speck
GO:0000151	ubiquitin ligase complex
GO:0030496	midbody
GO:0034399	nuclear periphery

Fig. 6. Transcriptomic analysis. A) Volcano plot for Differentially expressed genes. Red dots marked up-regulated genes; Blue dots marked down-regulated genes. Top 15 genes with the highest abs (logFC) values were labeled. B) Heat map for showing the differentially expressed genes related to "inflammatory activation related genes" after MS@MCL treatment under lactate stimulation. C) GO enrichment bubble plot for all differentially expressed genes. Red circles represented Biological Pathway; blue circles represented Cellular Component; grey circles represented Molecular Function. Top 5 enrichment terms for each category were shown. D) KEGG enrichment analysis for studying the pathways of inflammatory activation. E) The top 1 PPI network cluster detected by cytoscape pluggin mcode. (For interpretation of the references to color in this figure legend, the reader is referred to the Web version of this article.)

suggesting the biosafety of manganese injection *in vivo* (Fig. S11). Then, radiographic changes were observed by X-ray and MRI. As shown in Fig. 7B, the decrease in the DHI of MS@MCL groups was not obvious, which was similar to that of the shame group at different time points; however, the DHI rapidly collapsed in the NC group. Although the DHI of MCL group was similar to that of MS@MCL at 4 weeks, the DHI of five groups varied, with significantly narrowing in MS and MCL group at 8 weeks, suggesting that MS and MCL alone had little or no effect for IDD regeneration in lactate accumulation microenvironment for the long term (Fig. 7D and E). The MRI can reflect the water content of IVD, and the higher T2-weighted signal indicates higher water content of the NP tissues [33]. Herein, MRI results showed a significant low T2-weighted signal in the control group, while the signal strength always maintained high in the shame group at 4 and 8 weeks, respectively. The MCL and MS groups all showed a decrease in the T2-weighted signal at 8 weeks, but there was no significant difference in the MRI grading

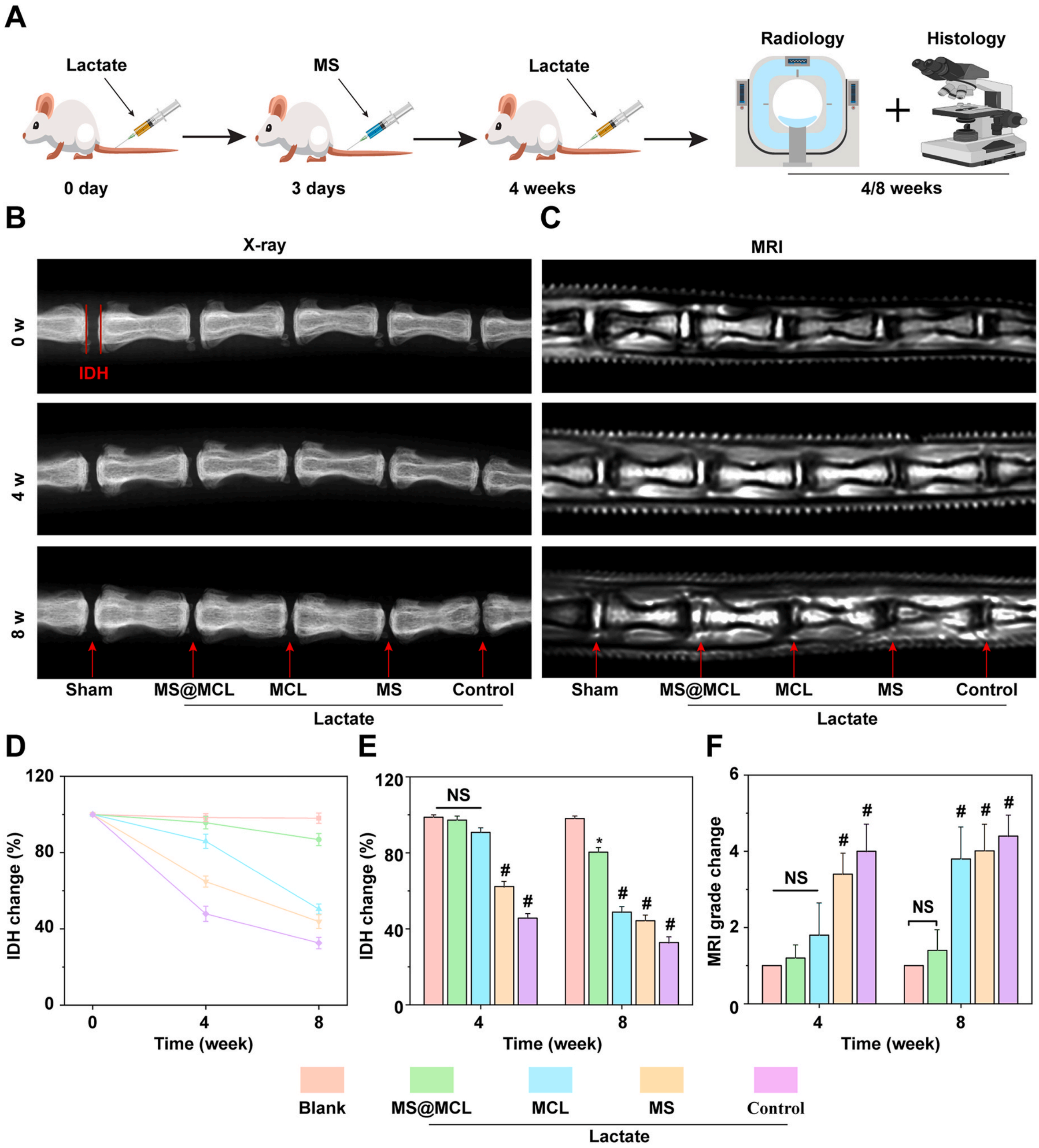

Fig. 7. Radiological evaluation of animal experiments. A) Schematic diagram of establishing lactate-induced rat IDD model and MS@MCL injection treatment. B, C) X-ray and MRI images of rat caudal vertebrae after different treatment at 0 week, 4 weeks and 8 weeks, respectively. D, E) The quantitative analysis of IDH changes in different groups at 4 and 8 weeks after molding. F) The quantitative analysis of MRI grade changes in different groups at 4 and 8 weeks after molding. *p < 0.05 Vs. blank group, $^{\#}p < 0.001$ Vs. MS@MCL group, NS Vs. MS@MCL group, not significant.

between the MS@MCL and MCL group at 4 weeks. At 8 weeks, the T2-weighted signal of the MS@MCL group kept the same intensity with that of the shame group, while the signal of the MCL and MS group continued to decrease (Fig. 7C and F).

To take further insight into the mechanism of MS@MCL application *in vivo*, histological sections were performed at 4 and 8 weeks. As revealed by HE and Safranin O-Fast Green staining, normal histological structure gradually disappeared and NP tissue atrophied over time in the control, MS and MCL groups compared with the sham group. Conversely, a clear tissue margins was still observed in MS@MCL group. Although a similar staining pattern was observed in the MCL group and MS@MCL group at 4 weeks, the NP tissue was gradually replaced by the annulus fibrosus at 8 weeks (Fig. 8A and B). The histological scores of the MS@MCL and MCL group were significantly lower than those in the MS and control group, similar to that in the shame group at 4 weeks; however, the score of the MCL group got worse over time, and showed a significant increase compared with that in the MS@MCL group at 8 weeks (Fig. 8C and D). Finally, to prove the MS@MCL regenerative effect via anti-inflammation, the expressions of collagen type II and IL-1β were evaluated by immunohistochemistry. The signal intensity of collagen type II was strongest in the MS@MCL group, compare with those observed in the other lactate-treated groups (Fig. 9A). However, the opposite trend of IL-1β signal intensity was observed (Fig. 9B). The results of semi-quantitative analysis were consistent with the staining observation (Fig. 9C and D). In summary, these results suggested that MCL alone could not play a long-term protective role *in vivo* partly

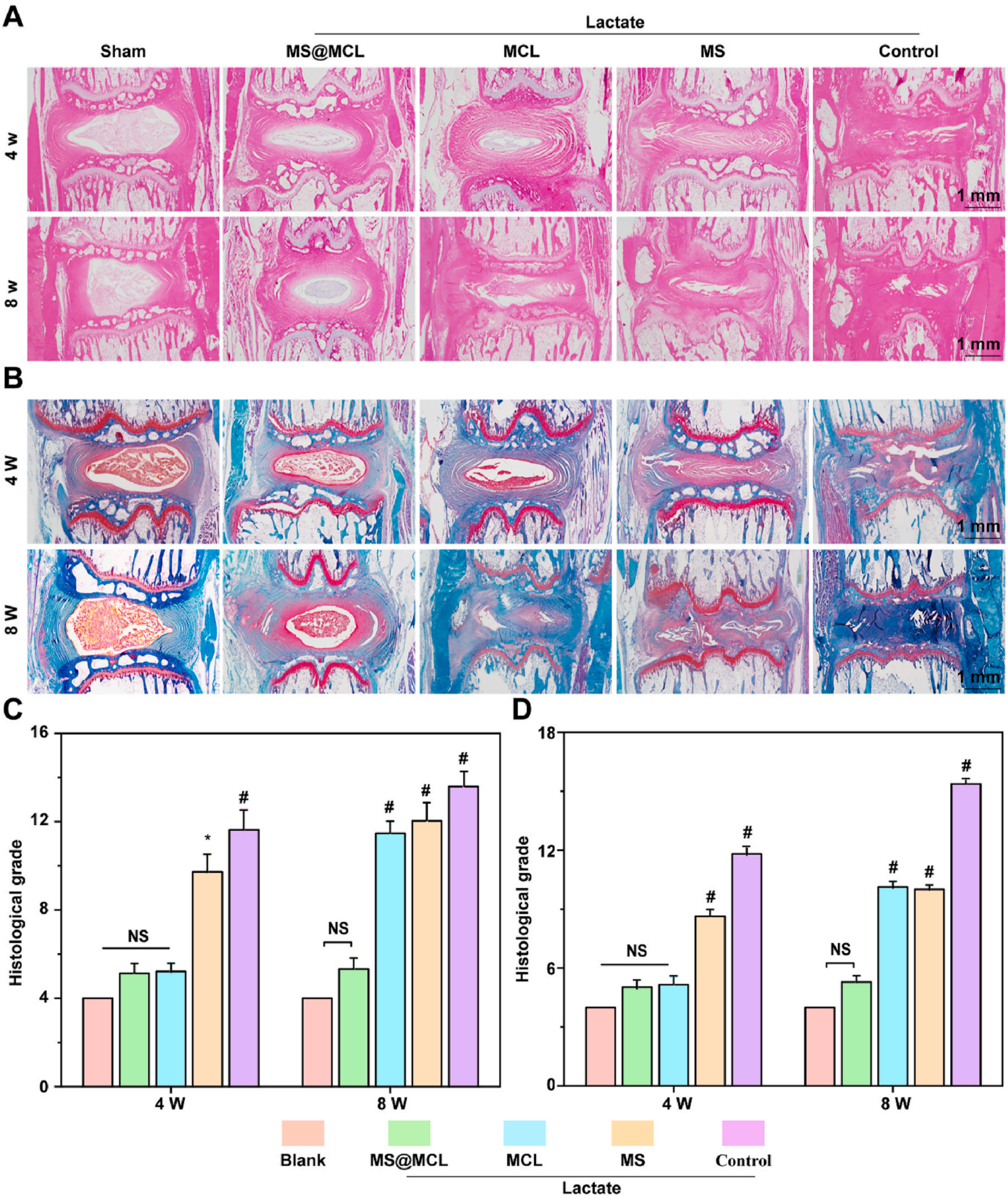

Fig. 8. Histological images of animal experiments. A, B) Representative images of H&E and Safranin O-fast green staining showing the histological changes of the NP tissues in different groups. C, D) Comparison of the histological grades in different groups at different time points. $^{*}p < 0.05$ Vs. blank group, $^{\#}p < 0.001$ Vs. MS@MCL group, NS Vs. MS@MCL group, not significant. (For interpretation of the references to color in this figure legend, the reader is referred to the Web version of this article.)

because the catalytic stability of free MCL NPs is worse than that of MCL immobilized onto microsphere in harsh scenarios. Furthermore, our nanozyme-functionalized hydrogel microsphere has some advantages such as easy production and storage, good injectability and long-term enzyme activity, whereas avoiding the drawback of short half-life for free nanozyme application *in vivo*.

4. Discussion

Since the discovery of the peroxidase (POD)-like activity of ferromagnetic nanoparticles in 2007 [34], different nanomaterials known as nanozymes have emerged as enzymatic mimetics. In the present study, the MnO_2 nanoplatform together with LOX constructe a composite nanozyme for lactate exhaustion through a cascade reaction to disrupt the lactate metabolism. Nanozymes have advantages of the regulatable catalytic activity, multi-functions and low cost [35]. However, the poor *in vitro* stability and short *in vivo* half-life of these exogenous nanomaterials remain an ongoing challenge for clinical application. In the present study, the covalent immobilization of nanozymes onto microspheres led to elevated enzyme stability due to the

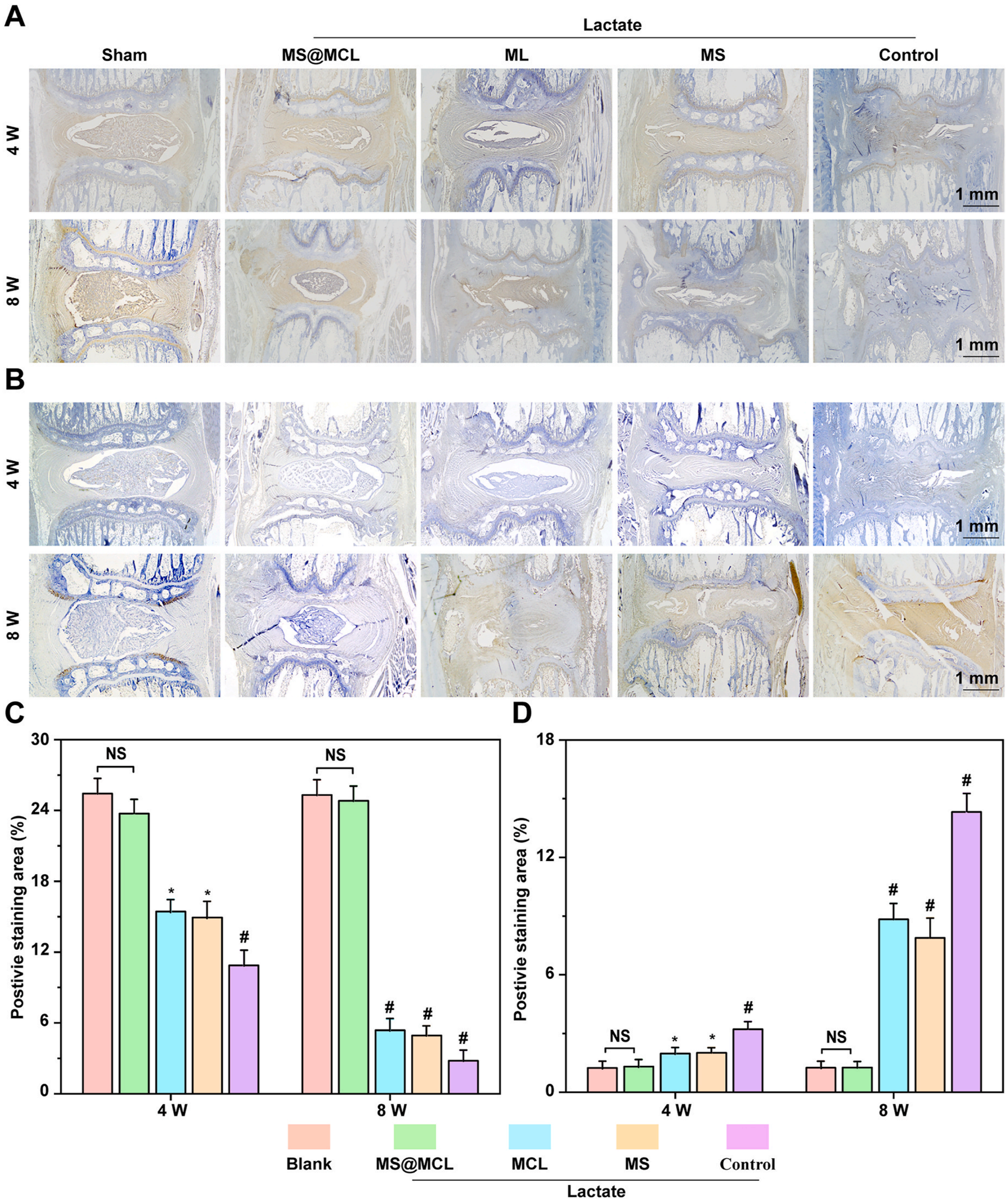

Fig. 9. Immunohistochemical analysis of COL-II and IL-1β expressions in rat NP. A) Immunohistochemical staining of COL-II at 4 weeks and 8 weeks. B) Immunohistochemical staining of IL-1β at 4 weeks and 8 weeks. C, D) The quantitative analysis of COL-II and IL-1β of different groups at 4 and 8 weeks after molding. $^{*}p < 0.05$ Vs. MS@MCL group, $^{\#}p < 0.001$ Vs. MS@MCL group, NS Vs. MS@MCL group, not significant.

promising robustness, avoiding leakage of protein from the surface of the nanomaterials [36]. Previous studies have reported the use of photo-crosslinked HAMA hydrogels for soft tissue regeneration, which could effectively protect, deliver and locally release bioactive factors [37]. However, large hydrogels are not always suited for their intended applications, particularly when injection is needed, or homogeneous sizes are required. More importantly, the tight internal cross-linked structure is not efficient for nanomaterials loading, whereas microgels prepared with microfluidic method exhibits several remarkable advantages over traditional hydrogels [38]: ① the size of microspheres is uniform and controlled, which is beneficial to *in situ* injection therapy; ② the porous structure of microspheres is suitable for encapsulation of bioactive molecules, which improves encapsulation efficiency of nanozymes. Thus, we prepared porous hydrogel microspheres based on heterogeneous size using a glass capillary microfluidic device. Herein, nanozymes could be encapsulated in hydrogel pores and remain stable inside. The nanozyme-functionalized hydrogel microsphere prepared by microfluidic technology leads to the controllable catalytic reaction and sustained release of nanoparticles [39].

The injectable nanozyme-functionalized hydrogel microsphere showed good effects on inflammation relief and tissue regeneration of NPCs in lactate enriched condition. Furthermore, the underlying biological mechanisms associated with the observed chondrogenic activities by exhausting local lactate accumulation were also studied by transcriptomic analysis. RNA contains all the necessary information required to mediate the expression of all biomolecules encoded by the cellular DNA. Recently, RNA sequencing technology has been widely used to assess the overall transcriptome changes in target tissues or cells, including splice junctions, novel transcripts, alternative splice variants, and un-annotated genes [40]. Thus, transcriptome changes in NPCs after exposure to MS@MCL were investigated. The KEGG enrichment analysis demonstrated that inflammation inhibited by MS@MCL catalytic microsystem mainly depended on the "P53", "MAPK", "cell cycle" and "peroxisome" pathways. The P53 protein is a transcription factor that controls a broad range of cellular processes including cell cycle arrest, DNA repair, and cellular metabolism. The activation of P53 is closely related to the onset of NPC senescence [41]. Recent study showed activation of Sirt1 might reduce P53 acetylation and potentially protect NP cells against apoptosis and senescence [42]. MAPK is a kind of serine threonine protein kinase in cells, which exists in most cells and exerts critical roles in hyper-inflammatory reactive diseases [43]. P Zhang et al. reported that inhibition of MAPK signaling pathway can induce proliferation and inhibit apoptosis of NPCs [44]. Over the past decades, peroxisomes have emerged as key regulators in overall cellular lipid and ROS metabolism [45]. Although the role of peroxisome in NPC remains unclear, the close relationship between peroxisome and mitochondria indicates a novel research perspective for pathogenesis of IDD [46]. The transcriptome sequencing results suggested that MS@MCL composites regulated mRNA expression in NPCs involving senescence, inflammation, cell cycle and cell structure, which is conducive to exploring the potential mechanism of this biomaterial on NPCs in lactate-rich condition.

5. Conclusion

In summary, the freeze-dried porous HAMA microsphere was covalently grafted with LOX-MnO_2 nanozyme to construct the injectable microsphere (MS@MCL) for repair and regeneration of the ischemic tissue. The uniform microspheres produced by microfluidic technology showed good injectability and biocompatibility while significantly increased the amount of enzyme loading by porous structure and maintained enzymatic concentration and activity by covalent bonding, achieving the long-term regulation of the microenvironment. Furthermore, it was demonstrated that this nanozyme-functionalized microsphere could down-regulate the local lactate level, reduce the expression of pro-inflammatory factors, protect cells from death, and enhance the synthesis of ECM, thus inhibiting the process of IDD and promoting IVD regeneration. This injectable nanozyme-functional microsphere provides a new idea for ischemic tissue regeneration in local extracellular lactate-accumulated microenvironment.

CRediT authorship contribution statement

Jieliang Shen: Conceptualization, Methodology, Validation, Formal analysis, Data curation, Writing – original draft, Visualization. **Ao Chen:** Methodology, Formal analysis, Visualization. **Zhengwei Cai:** Methodology, Visualization. **Zhijie Chen:** Methodology, Software, Formal analysis. **Ruichao Cao:** Methodology. **Zongchao Liu:** Resources, Writing – review & editing. **Yuling Li:** Conceptualization, Methodology, Validation, Investigation, Writing – original draft, Supervision, Project administration. **Jie Hao:** Conceptualization, Methodology, Validation, Investigation, Writing – original draft, Supervision, Project administration, Funding acquisition.

Declaration of competing interest

The authors declare that the research was conducted in the absence of any commercial or financial relationships that could be construed as a potential conflict of interest.

Acknowledgement

This study was financially supported by the National Natural Science Foundation of China (82102578, 81922045, 81772314 and 21604052), the National Natural Science Foundation of Chongqing (cstc2018jcyjAX0059 and cstc2018jcyjAX0797), Applied Basic Research Programs of the Science and Technology Department of Sichuan Province (2021YJ0467). All protocols of the animal study were approved by the institutional review committee of Shanghai Jiao Tong University.

Appendix A. Supplementary data

Supplementary data to this article can be found online at https://doi.org/10.1016/j.bioactmat.2021.10.013.

References

[1] J.D. Rabinowitz, S. Enerback, Lactate: the ugly duckling of energy metabolism [J], Nat Metab 2 (7) (2020) 566–571.

[2] D. Zhang, Z. Tang, H. Huang, et al., Metabolic regulation of gene expression by histone lactylation [J], Nature 574 (7779) (2019) 575–580.

[3] G.A. Brooks, The science and translation of lactate shuttle theory [J], Cell Metabol. 27 (4) (2018) 757–785.

[4] L.B. Ivashkiv, The hypoxia-lactate axis tempers inflammation [J], Nat. Rev. Immunol. 20 (2) (2020) 85–86.

[5] V. Pucino, M. Bombardieri, C. Pitzalis, et al., Lactate at the crossroads of metabolism, inflammation, and autoimmunity [J], Eur. J. Immunol. 47 (1) (2017) 14–21.

[6] J.C. Garcia-Canaveras, L. Chen, J.D. Rabinowitz, The tumor metabolic microenvironment: lessons from lactate [J], Cancer Res. 79 (13) (2019) 3155–3162.

[7] H. Choi, C. Merceron, L. Mangiavini, et al., Hypoxia promotes noncanonical autophagy in nucleus pulposus cells independent of MTOR and HIF1α signaling [J], Autophagy 12 (9) (2016) 1631–1646.

[8] V. Madhu, P.K. Boneski, E. Silagi, et al., Hypoxic regulation of mitochondrial metabolism and mitophagy in nucleus pulposus cells is dependent on HIF-1alpha-BNIP3 axis [J], J. Bone Miner. Res. 35 (8) (2020) 1504–1524.

[9] S. Yang, F. Zhang, J. Ma, et al., Intervertebral disc ageing and degeneration: the antiapoptotic effect of oestrogen [J], Ageing Res. Rev. 57 (2020) 100978.

[10] E.S. Silagi, Z.R. Schoepflin, E.L. Seifert, et al., Bicarbonate recycling by HIF-1-dependent carbonic anhydrase isoforms 9 and 12 is critical in maintaining intracellular pH and viability of nucleus pulposus cells [J], J. Bone Miner. Res. 33 (2) (2018) 338–355.

[11] J. Shi, X. Zhou, Z. Wang, et al., Increased lactic acid content associated with extracellular matrix depletion in a porcine disc degeneration induced by superficial annular lesion [J], BMC Muscoskel. Disord. 20 (1) (2019) 551.

[12] K.R. Keshari, J.C. Lotz, T.M. Link, et al., Lactic acid and proteoglycans as metabolic markers for discogenic back pain [J], Spine 33 (3) (2008) 312–317.

[13] V.A. Byvaltsev, S.I. Kolesnikov, L.A. Bardonova, et al., Assessment of lactate production and proteoglycans synthesis by the intact and degenerated intervertebral disc cells under the influence of activated macrophages: an in vitro study [J], Bull. Exp. Biol. Med. 166 (1) (2018) 170–173.

[14] F. Alam, S. Roychoudhury, A.H. Jalal, et al., Lactate biosensing: the emerging point-of-care and personal health monitoring [J], Biosens. Bioelectron. 117 (2018) 818–829.

[15] C. Feng, M. Yang, M. Lan, et al., ROS: Crucial Intermediators in the Pathogenesis of Intervertebral Disc Degeneration [J], vol. 2017, Oxid Med Cell Longev, 2017, p. 5601593.

[16] B. Ding, P. Zheng, P. Ma, et al., Manganese oxide nanomaterials: synthesis, properties, and theranostic applications [J], Adv. Mater. 32 (10) (2020), e1905823.

[17] S.A. Ansari, Q. Husain, Potential applications of enzymes immobilized on/in nano materials: a review [J], Biotechnol. Adv. 30 (3) (2012) 512–523.

[18] Z. Ashkan, R. Hemmati, A. Homaei, et al., Immobilization of enzymes on nanoinorganic support materials: an update [J], Int. J. Biol. Macromol. 168 (2021) 708–721.

[19] F. Zhang, X. Liu, B. Li, et al., The effect of hyaluronic acid on nucleus pulposus extracellular matrix production through hypoxia-inducible factor-1alpha transcriptional activation of CD44 under hypoxia [J], Eur. Cell. Mater. 41 (2021) 142–152.

[20] S. Aggarwal, A. Chakravarty, S. Ikram, A comprehensive review on incredible renewable carriers as promising platforms for enzyme immobilization & thereof strategies [J], Int. J. Biol. Macromol. 167 (2021) 962–986.

[21] C. Zhou, C. Gao, Z. Lin, et al., Autonomous motion of bubble-powered carbonaceous nanoflask motors [J], Langmuir 36 (25) (2020) 7039–7045.

[22] W. Pan, Y. Ge, Z. Yu, et al., A cancer cell membrane-encapsulated MnO2 nanoreactor for combined photodynamic-starvation therapy [J], Chem. Commun. 55 (35) (2019) 5115–5118.

[23] J. Bian, F. Cai, H. Chen, et al., Modulation of local overactive inflammation via injectable hydrogel microspheres [J], Nano Lett. 21 (6) (2021) 2690–2698.

[24] J. Zou, Selection of the optimal puncture needle for induction of a rat intervertebral disc degeneration model[J], Pain Physician 22 (2019) 353–360.

[25] S. Bhavaniramya, R. Vanajothi, S. Vishnupriya, et al., Enzyme immobilization on nanomaterials for biosensor and biocatalyst in food and biomedical industry [J], Curr. Pharmaceut. Des. 25 (24) (2019) 2661–2676.

[26] Y. Zhang, H. Wang, X. Jia, et al., Cascade catalytic nanoplatform for enhanced starvation and sonodynamic therapy [J], J. Drug Target. 28 (2) (2020) 195–203.

[27] Z.Y. Xie, L. Chen, F. Wang, et al., Endoplasmic reticulum stress is involved in nucleus pulposus degeneration and attenuates low pH-induced apoptosis of rat nucleus pulposus cells [J], DNA Cell Biol. 36 (8) (2017) 627–637.

[28] C.Y. Huang, W.Y. Gu, Effects of mechanical compression on metabolism and distribution of oxygen and lactate in intervertebral disc [J], J. Biomech. 41 (6) (2008) 1184–1196.

[29] K. Zhao, R. An, Q. Xiang, et al., Acid-sensing ion channels regulate nucleus pulposus cell inflammation and pyroptosis via the NLRP3 inflammasome in intervertebral disc degeneration [J], Cell Prolif 54 (1) (2021), e12941.

[30] E.S. Silagi, I.M. Shapiro, M.V. Risbud, Glycosaminoglycan synthesis in the nucleus pulposus: dysregulation and the pathogenesis of disc degeneration [J], Matrix Biol. 71–72 (2018) 368–379.

[31] Y. Wang, M. Che, J. Xin, et al., The role of IL-1 beta and TNF-alpha in intervertebral disc degeneration [J], Biomed. Pharmacother. 131 (2020) 110660.

[32] M. Certo, C.H. Tsai, V. Pucino, et al., Lactate modulation of immune responses in inflammatory versus tumour microenvironments [J], Nat. Rev. Immunol. 21 (3) (2021) 151–161.

[33] Y.J. Che, J.B. Guo, T. Liang, et al., Assessment of changes in the micro-nano environment of intervertebral disc degeneration based on Pfirrmann grade, J. Spine J 19 (7) (2019) 1242–1253.

[34] L. Gao, J. Zhuang, L. Nie, et al., Intrinsic peroxidase-like activity of ferromagnetic nanoparticles [J], Nat. Nanotechnol. 2 (9) (2007) 577–583.

[35] Y. Huang, J. Ren, X. Qu, Nanozymes: classification, catalytic mechanisms, activity regulation, and applications [J], Chem. Rev. 119 (6) (2019) 4357–4412.

[36] V.L. Sirisha, A. Jain, A. Jain, Enzyme immobilization: an overview on methods, support material, and applications of immobilized enzymes [J], Adv. Food Nutr. Res. 79 (2016) 179–211.

[37] B.S. Spearman, N.K. Agrawal, A. Rubiano, et al., Tunable methacrylated hyaluronic acid-based hydrogels as scaffolds for soft tissue engineering applications [J], J. Biomed. Mater. Res. 108 (2) (2020) 279–291.

[38] W. Li, L. Zhang, X. Ge, et al., Microfluidic fabrication of microparticles for biomedical applications [J], Chem. Soc. Rev. 47 (15) (2018) 5646–5683.

[39] J. Mujtaba, J. Liu, K.K. Dey, et al., Micro-Bio-Chemo-Mechanical-Systems: micromotors, microfluidics, and nanozymes for biomedical applications [J], Adv. Mater. 33 (22) (2021), e2007465.

[40] Z. Wang, M. Gerstein, M. Snyder, RNA-Seq: a revolutionary tool for transcriptomics [J], Nat. Rev. Genet. 10 (1) (2009) 57–63.

[41] C.C. Chen, J. Chen, W.L. Wang, et al., Inhibition of the P53/P21 pathway attenuates the effects of senescent nucleus pulposus cell-derived exosomes on the senescence of nucleus pulposus cells [J], Orthop. Surg. 13 (2) (2021) 583–591.

[42] Z. Zhang, J. Lin, M. Nisar, et al., The Sirt1/P53 axis in diabetic intervertebral disc degeneration pathogenesis and therapeutics [J], Oxid Med Cell Longev 2019 (2019) 7959573.

[43] J.S. Arthur, S.C. Ley, Mitogen-activated protein kinases in innate immunity [J], Nat. Rev. Immunol. 13 (9) (2013) 679–692.

[44] P. Zhang, B.G. Chang, Inhibitory effect on the apoptosis of disc nucleus pulposus cells in rats by silencing COL9A3 gene to mediate MAPK signaling pathway: a study on the function and mechanism [J], Eur. Rev. Med. Pharmacol. Sci. 24 (17) (2020) 8653–8664.

[45] J.A. Kim, Peroxisome metabolism in cancer [J], Cells 9 (7) (2020) 1692.

[46] K. Sun, X. Jing, J. Guo, et al., Mitophagy in degenerative joint diseases [J], Autophagy (2020) 1–11.